Research Article

Robust enhanced hydrogen production at acidic conditions over molybdenum oxides-stabilized ultrafine palladium electrocatalysts

Ji Sun[1,2,§], Xian Zhang[1,§], Meng Jin[1,2], Qizhong Xiong[1], Guozhong Wang[1], Haimin Zhang[1] (✉), and Huijun Zhao[1,3] (✉)

[1] Key Laboratory of Materials Physics, Centre for Environmental and Energy Nanomaterials, Anhui Key Laboratory of Nanomaterials and Nanotechnology, CAS Center for Excellence in Nanoscience Institute, Institute of Solid State Physics, Chinese Academy of Sciences, Hefei 230031, China
2 University of Science and Technology of China, Hefei 230026, China
3 Centre for Clean Environment and Energy, Griffith University, Gold Coast Campus, QLD 4222, Australia
§ Ji Sun and Xian Zhang contributed equally to this work.

ABSTRACT

Electrochemical water splitting is quite seductive for eco-friendly hydrogen fuel energy production, however, the attainment of highly efficient, durable, and cheap catalysts for the hydrogen evolution reaction (HER) remains challenging. In this study, molybdenum oxides stabilized palladium nanoparticle catalysts (MoO_x-Pd) are *in situ* prepared on commercial carbon cloth (CC) by the facile two-step method of dip-coating and electrochemical reduction. As a self-supported Pd-based catalyst electrode, the MoO_x-Pd/CC presents a competitive Tafel slope of 45.75 mV·dec^{-1}, an ultralow overpotential of 25 mV, and extremely long cycling durability (one week) in 0.5 M H_2SO_4 electrolyte, superior to unmodified Pd catalysts and comparable to commercial Pt mesh electrode. On the one hand, the introduction of MoO_x can inhibit the growth of Pd particles to obtain ultrafine Pd nanoparticles, thus exposing more available active sites. On the other hand, density functional theory (DFT) calculation revealed that MoO_x on the surface of Pd metal can regulate the electronic structure of Pd metal and enhance its intrinsic catalytic activity of HER. This work suggests that transitional metal nanoparticles stabilized by molybdenum oxides are hopeful approaches for obtaining fruitful hydrogen-producing electrocatalysts.

KEYWORDS

MoO_x, Pd nanoparticles, electrocatalysts, hydrogen evolution reaction

1   Introduction

The status quo of energy scarcity and environmental imbalance and unsustainability caused by tremendously consumed fossil fuels has been deteriorating at an alarming rate. So it is imminent and essential for us to replace traditional fuels with a green renewable energy source. Hydrogen, a clean-burning energy resource of high energy density, is acknowledged as the promising fuel due to its plenitude, renewability, and remarkable efficiency [1, 2]. Among lots of advisable approaches to attaining green fuel energy of hydrogen gas, electrochemical water splitting has drawn broad attention and has been researched and discussed extensively, owing to its proficient ability to utilize discontinuous energy by transforming regenerable electricity to hydrogen energy ecofriendly [3–5]. At present, the alkaline electrolyzer is the most universal facility to hydrogen [6]. However, the ability of such a device is constrained by the slow rate of hydrogen evolution kinetics of the reaction resulting from huge ohmic resistance of alkaline electrolyte and high overpotential drawbacks [7]. These issues are addressed in the wake of proton exchange membrane (PEM) electrolyzers, operating well in acidic electrolytes. Unfortunately, the wide-ranging application of PEM in electrochemical water splitting is limited by the scantiness of

productive, durable and simply prepared electrocatalysts for hydrogen evolution reaction (HER) [8, 9]. The past decades have witnessed multiple signs of progresses of HER catalysts materials, among which commercial Pt/C is the benchmarking catalyst [10]. Platinum-group elements supported catalysts have shown good results in HER reactions, being active even at low temperatures [11, 12]. These noble metals are intriguing due to their capability to furnish active sites for hydrogen evolution while they are less recipient to deactivation by water; therefore, longer life spans of the catalysts are anticipated [13, 14]. However, the resource-deficient Pt element severely limits its large-scale application in electrocatalytic HER. Compared with expensive platinum, palladium possesses richer resources [15]. However, from the perspective of the volcanic diagram [16], Pd has stronger hydrogen adsorption than Pt, resulting in weaker hydrogen production performance. Therefore, the key to develop Pd-based catalysts is to regulate the electronic structure of Pd to weaken its hydrogen adsorption, so that produce higher catalytic performance. This gives the catalytic system piles of superiorities such as the possibility of large scale manufacturing of ameliorated materials provided with the acceptable electrocatalytic ability and ascending utilization rate; this thus reduces the demand of platinum catalyst and integrally shrinks catalyst cost [13, 17]. Hence, to fulfill the

Address correspondence to Haimin Zhang, zhanghm@issp.ac.cn; Huijun Zhao, h.zhao@griffith.edu.au

requirements of practical application, it is strongly intended to research non-platinum based electrocatalysts with superb catalytic properties, specifically outstanding hydrogen production performance and competitive durability at acidic conditions.

Employing metal oxide support is considered as an effective way to promote the electrocatalytic activity of metal-based catalyst [18]. Because the metal catalyst supported on the metal oxide surface can prevent the metal nanoparticles agglomeration and obtain ultrafine metal particles, thus improving the exposed catalytic active sites [19]. Moreover, the incorporation of appropriate oxides can effectively alter the electronic structures of metallic particles by synergistic effect and then affect their catalytic properties [19]. In this regard, molybdenum oxide is a promising candidate. This is due to the excellent electronic conductivity and fine stability of molybdenum oxides in acidic solutions [20]. However, the preparation methods of nano-sized metal-based catalysts, including solvothermal reduction, liquid reduction method, heat treatment reduction and so forth, all go through tedious centrifugation, washing, or coating process of catalyst electrode, which is not conducive to large-scale commercial applications. Recently, self-supported catalysts are advisable for avoiding the indispensability of adhesive while attaching traditional powdery particles to the electrode, enabling swift charge and mass transport [21], which have hardly been discussed for HER in acidic condition [22, 23].

In the work presented here, a self-supported MoO_x-stabilized ultrafine palladium electrocatalyst on carbon cloth (denoted as MoO_x-Pd/CC) was acquired to attain excellent catalytic efficiency for the electrochemical HER in acidic condition. The MoO_x-Pd/CC catalyst is synthesized by a facile two-step method of dip-coating and electrochemical reduction. The consequential MoO_x-Pd/CC embraces higher intrinsic activity than the bare palladium particles supported on CC (Pd/CC) and the bare molybdenum oxides grown on CC (MoO_x/CC). Outstandingly, MoO_x-Pd/CC exhibits an ultralow overpotential of 25 mV at 10 mA·cm^{-2}, surpassing the majority of the declared HER electrocatalysts in acidic solutions. Moreover, robust durability is attained as well, with a progressive overpotential decrease after a successive electrocatalysis of 7 days. Further characterization and density functional theory (DFT) calculation results showed that ultrafine Pd nanoparticles could be obtained *in situ* by using MoO_x loading, and MoO_x on the surface of Pd nanoparticles could regulate the electronic structure of Pd surface to enhance their intrinsic HER catalytic activity. This study provides a new study strategy for large-scale construction of metal-based hydrogen-producing electrocatalysts with high efficiency and low load.

2 Experimental section

2.1 Materials

Palladium chloride ($PdCl_2$) and molybdenum pentachloride ($MoCl_5$) were acquired from Sinopharm Chemical Reagent Co., Ltd. The commercial platinum mesh was purchased from Gaoss Union Co., Ltd. Sulphuric acid (H_2SO_4, AR) and nitric acid (AR) were attained from Macklin reagent Co., Ltd. The carbon cloth was attained and immersed in nitric acid (AR) at 80°C for 4 h to promote its hydrophilicity before processing. Deionized water was utilized during the entire experiment.

2.2 Synthesis of MoO_x-Pd/CC

Firstly, 4 mg $PdCl_2$ and 9 mg $MoCl_5$ became incorporated into 20 mL of industrial alcohol under magnetic stirring for 4 h. The uniform obtained solution remained still for later utilization. Next, a piece of CC (1.0 cm × 2.0 cm) was soaked into the

prepared solution for around 10 s and then picked out. After drying under a normal blow dryer, the processed carbon cloth was served as a cathode for three-electrode system in 0.5 M electrolyte of H_2SO_4 during linear sweep voltammetry (LSV) when Mo species were reduced and hydrogen began to be brought out. Until the curve of LSV was settled, the electrode was taken off and immersed again into the precursor solution after a simple rinse by industrial alcohol. After this, the electrode was applied for LSV again. The entire process was repeated several times until achieving the superior electrochemical properties. As for the preparation of MoO_x/CC and Pd/CC, bare 9 mg $MoCl_5$ or 4 mg $PdCl_2$ was employed for the corresponding precursor solution, respectively. The typical metal mass loading of MoO_x/CC, Pd/CC, and MoO_x-Pd/CC were tested and then calculated to be 4.392, 6.856, and 4.514 µg·cm^{-2}, respectively, using Thermo Fisher Scientific icp6300 spectrometer.

2.3 Characterizations

The X-ray diffraction (XRD) analyses of all electrodes were performed on a PANalytical X'Pert diffractometer with Cu Kα radiation (λ = 1.5418 Å). Besides, the scanning electron microscopy (SEM) figures were attained from a Hitachi SU8020 field emission scanning electron microscope. And an FEI Tecnai G2 F20 microscope was utilized for the images of the transmission electron microscopy (TEM) and high-resolution TEM (HRTEM), which produced energy-dispersive X-ray spectroscopy (EDS) results simultaneously. For detailed TEM, HRTEM, and EDS examination, the electrode material powder was removed from CC using scrapers and then underwent ultrasonic dispersion. The X-ray photoelectron spectroscopy (XPS) results were taken from a Shimadzu/Kratos AXIS Ultra XPS spectrometer. The Raman spectra was acquired from a Renishaw inVia Reflex Raman microscope. The electron spin resonance (ESR) outcomes were presented by a Bruker EMX plus analyzer (298 K, 9.87 GHz).

2.4 Electrochemical measurements

The electrocatalytic properties of all electrodes were investigated using a CHI 760E electrochemical workstation from CH Instruments, Inc. in a three-electrode system. The as-synthesized samples worked as the working electrode, while a saturated Ag/AgCl electrode and a piece of carbon paper (1.0 cm × 2.0 cm) were served as the reference electrode and the counter electrode, respectively. All the measurements of electrochemical performances were carried out in 0.5 M H_2SO_4. The current densities of the results were computed in regard to the valid area of the working electrodes (1.0 cm × 1.0 cm). And the potential was reflected, relative to reversible hydrogen electrode (RHE), in experimental consequences unless a particular declaration. The LSV curves were conducted and collated in the potential range of −0.8–0.2 V vs. RHE. In addition, the electrochemical impedance spectroscopy (EIS) mensurations were carried out with a 10 mV amplitude and a frequency range from 100 kHz to 0.1 Hz. Besides, the chronopotentiometry (CP) test at 10 mA·cm^{-2} was employed to investigate the stability of the electrode.

To determine the electrochemical active surface area (ECSA) of prepared catalyst electrode, the prepared samples were ground into powder respectively and then specific catalyst ink was prepared by dispersing 15 mg powder in the uniform solution consisting of 1 mL distilled water, 1 mL ethanol, and 40 µL of 5 wt.% Nafion solution. Each suspension was sonicated for 30 min before coating the glass carbon electrode. 30 µL catalyst ink was drop casted on glass carbon electrode and followed by drying up at 40 °C for 10 min. The catalyst ink coating on the glass carbon electrode was utilized as a working

electrode, a platinum wire was served as a counter electrode, and a saturated Ag/AgCl electrode was adopted as a reference electrode. The CV curves of the catalysts were investigated by using rotating disc electrode (RDE) in N_2 saturated 0.5 M H_2SO_4 at 50 mV·s^{-1}. The ECSA of the electrode was evaluated by charge under hydrogen desorption peak from the recorded CV curve, presuming a charge density of 210 μC·cm^{-2} for one monolayer of hydrogen coverage on Pd/CC and MoO$_x$-Pd/CC. The formula for ECSA of the electrode catalyst is listed in the Electronic Supplementary Material (ESM). Each experiment was accomplished at 25 °C.

2.5 DFT calculation

All simulations were finished using the Vienna *ab initio* simulation package (VASP). The projector augmented wave (PAW) potential and the plane-wave cut-off energy of 450 eV were used within a Perdew–Burke–Ernzerhof (PBE) generalized gradient approximation (GGA) to the exchange and correlation functional. For the surface calculations, a p (4×4) surface unit cell was adopted to constitute a four-layer metal slab. The Brillouin zone was sampled using a 2×2×1 Gamma centered Monkhorst-Pack mesh. During the geometry optimization, the top two layers of the slab were fixed while the others were allowed to relax. The energies were converged to e^{-4}, and ionic relaxations were allowed until all forces were smaller than 0.05 eV/Å.

3 Result and discussion

The synthetic scheme of MoO$_x$ stabilized ultrafine Pd nanoparticles embedded into the carbon cloth (denoted as MoO$_x$-Pd/CC) is displayed in Fig. 1. To begin with, a piece of commercial carbon cloth was submerged into a uniform industrial alcohol solution containing PdCl$_2$ and MoCl$_5$. After taking away from the liquid mixture and drying, the received CC electrode was executed electrochemical reduction. Pd/CC and MoO$_x$/CC were prepared with the similar method.

The structure and composition of the as-synthesized catalyst electrodes were further characterized by lots of characterizations, including XRD, Raman, SEM, TEM, XPS, and ESR. In the XRD pattern of MoO$_x$/CC electrode (Fig. 2(a)), two broadened peaks focused at 24.9° and 43.2° are found and belonged to the reflection of graphitic carbon from the CC substrate [24], while an extremely weak peak noticed at 26.1° should be ascribed to (11$\bar{1}$) plane of MoO$_2$ (PDF # 96-900-9091), as shown in Fig. S1 in the ESM. Comparatively, there is a similar signal of MoO$_2$ in the XRD pattern of MoO$_x$-Pd/CC. Other characteristic peaks of MoO$_x$ are so humble that they obliterate in the background signal, indicating that the majority of them could not assemble as crystalline aggregation and the content is low [25, 26]. The XRD pattern for Pd/CC shows three characteristic peaks corresponding to palladium crystal of typical cubic structure at 2θ = 40.1°, 46.6°, 68.1°, appointing to the (111), (002) and (022) planes of Pd (PDF # 96-900-8479), respectively. Figure 2(a) clearly exhibits that diffraction peaks of MoO$_x$-Pd/CC are further weaker than that of Pd/CC. In the light of the Debye-Scherrer equation, the higher full width at half-maximum of MoO$_x$-Pd/CC indicates that Pd particles of

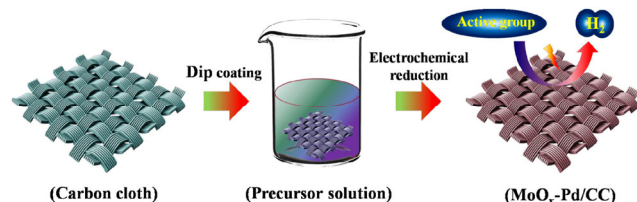**Figure 1** Schematic illustration of the synthetic procedure of MoO$_x$-Pd/CC.

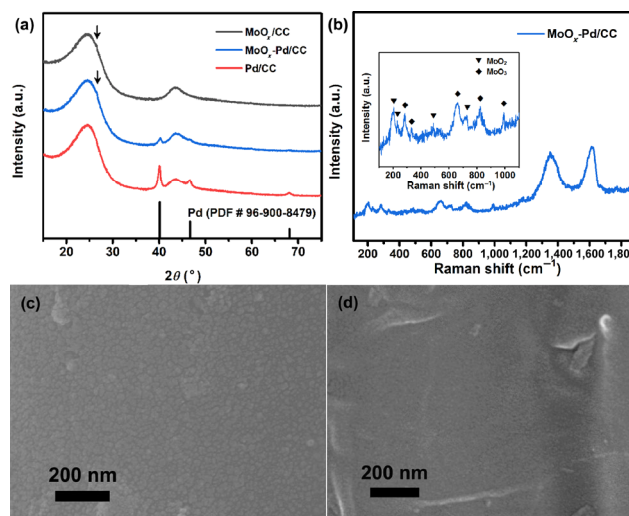**Figure 2** (a) XRD patterns of MoO$_x$/CC, MoO$_x$-Pd/CC and Pd/CC electrodes. (b) Raman spectrum of MoO$_x$-Pd/CC electrode. SEM images of Pd/CC (c) and MoO$_x$-Pd/CC (d) electrode.

MoO$_x$-Pd/CC have a smaller average particle dimension [27]. Hence, it could be justified that the crystallinity of palladium particles can be efficaciously shrunk by the introduction of MoO$_x$, indicative of high dispersion of the loaded species. Additionally, signals of palladium are slightly shifted to higher Bragg angles in contrast to that of Pd/CC. Thus, the crystal structure of palladium is assumed to be transformed by the interference of MoO$_x$.

The Raman spectrum of MoO$_x$-Pd/CC as shown in Fig. 2(b) reveals two big bands at 1,355 and 1,612 cm^{-1}, referring to as D and G of CC; it also clearly shows a series of small peaks on the left-hand side of the Raman signal ranging from 100 to 1,100 cm^{-1}: several peaks located at 203, 227, 486, and 727 cm^{-1} verify the existence of MoO$_2$, while signals at 285, 334, 662, 819, and 992 cm^{-1} are responses derived from MoO$_3$ [28]. The measured peaks pointed to Mo oxides are mighty feeble, justifying the low crystallinity of Mo oxides. Additionally, almost all of them slightly deviate from the standard spectrum of MoO$_2$ and MoO$_3$ (Fig. S2 in the ESM), rendering the presence of transitional status of Mo oxides possible. Moreover, there is no obvious peak relative to palladium species as expected. Further, the SEM was employed to inspect the load of MoO$_x$ and Pd-based particles on the CC. As represented in the SEM image of Pd/CC (Fig. 2(c)), Pd particles are distributed on CC and the electrode exhibits rough surface. Contrarily, the MoO$_x$-Pd/CC electrode displays a smooth surface probably resulting from the even distribution of MoO$_x$-Pd nanoparticles in Fig. 2(d). Addtionally, the SEM image of MoO$_x$/CC is provided (Fig. S3 in the ESM), there is no evident particles of MoO$_x$ on the CC, due to its low crystallinity and high dispersion.

Also the TEM was utilized for investigating the effect of MoO$_x$ toward electrocatalyst morphology. Figures 3(a) and 3(b) show the TEM images of the Pd/CC sample. According to the selected area electron diffraction (SAED) pattern of Pd/CC (Fig. 3(b), inset), three distinguishing Debye rings respectively correspond to the (111), (002), and (022) planes of Pd, which is in accordance with the HRTEM image presented in Fig. 3(c). As displayed in Figs. 3(b) and 3(c), Pd nanocrystals of Pd/CC stay as aggregates of particles ranging from 5–20 nm in diameter. Compared to the Pd/CC (Fig. 3(b), inset), the wider rings of MoO$_x$-Pd/CC (Fig. 3(e), inset) can be imputed to the more diminutive particle size and the lower crystallinity [29]. This result is further demonstrated by Fig. 3(e), which shows the size distribution of 1–4 nm for MoO$_x$-stabilized Pd nanoparticles.
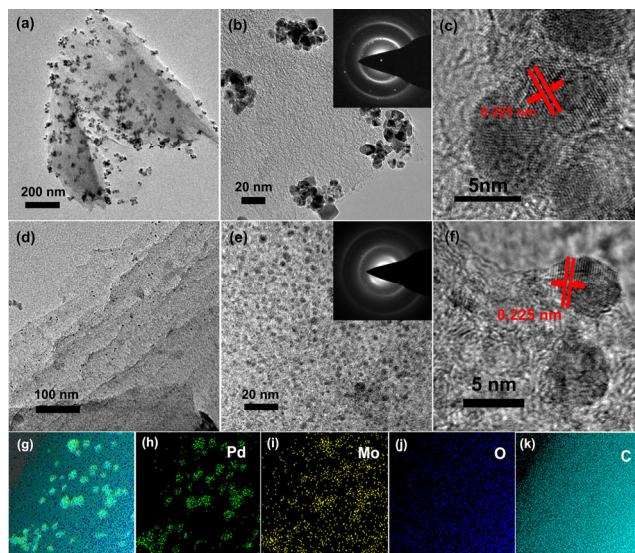
Figure 3 (a) and (b) TEM images of Pd/CC, the inset of (b) shows the SEAD pattern of Pd/CC. (c) Enlarged HRTEM image of Pd/CC. (d) and (e) TEM images of MoO$_x$-Pd/CC, the inset of (e) shows the SEAD pattern of MoO$_x$-Pd/CC. (f) Enlarged HRTEM image of MoO$_x$-Pd/CC. (g)–(k) EDS element mapping of MoO$_x$-Pd/CC.

However, the patterns of Mo oxides remain obscure and indeterminate, owing to that they exist in highly amorphous form and that the optimally oriented plane ($11\bar{1}$) of MoO$_2$ (as shown in the inset of Fig. 3(e)) retains similar interplanar spacing (0.34 nm) with that of carbon cloth (0.36 nm), presenting entirely as one wide and dizzy annulus close to the center of the rings. Figure 3(f) displays corresponding lattice fringes identified as the (111) facet of Pd nanoparticles, which further proves that ultrafine nanocrystals are Pd nanoparticles. Besides, the TEM image of MoO$_x$/CC is displayed in Fig. S4 in the ESM. Amplified HRTEM image of MoO$_x$-Pd nanoparticles is also demonstrated in Fig. S5 in the ESM, where MoO$_x$ composition of catalyst and tiny Pd particles spread out through the carbon matrix. Therefore, the addition of Mo oxides is beneficial for Pd particles to minimize their size and grow disjointedly. Predictably, such tiny nanoparticles are gainful for exposing more active sites and upgrading HER performance. The involved content analyses of the elements of MoO$_x$-Pd/CC were investigated by EDS in Fig. S6 in the ESM. Because of the low metal loading, an inductively coupled plasma (ICP) spectrometer was utilized to ascertain the specific content of the catalysts ulteriorly (Table S1 in the ESM). Besides, the elemental mapping images (Figs. 3(g)–3(k)) further manifest that Pd nanoparticles are uniformly dispersed and Mo species locate discretely throughout CC, relatively enriched around Pd particles.

To attain further insights into the compositional transmutation of MoO$_x$-Pd catalysts during electrochemical reduction, XPS tests were also applied (Fig. 4 and Fig. S7 in the ESM). As shown in Fig. 4(a), the catalyst electrode before electrochemical reduction displays the Pd 3d$_{5/2}$ and Pd 3d$_{3/2}$ signals connected to metallic palladium at binding energies of 335.7 and 340.9 eV and another group of signals generated by Pd^{2+} of chloride at 338.0 and 343.3 eV [30]. In comparison, that Pd^{2+} is reverted to metallic Pd after electrochemical reaction and the binding energies of metallic Pd shift to higher status (335.8 and 341.0 eV) are observed in Fig. 4(b). In contrast to catalyst before electrochemical reaction which only exhibits two bands of Mo^{6+} at 233.1 and 236.3 eV in Fig. 4(c), the sample after reduction presents two accessional pairs of Mo 3d$_{5/2}$ and Mo 3d$_{3/2}$ peaks associated with Mo^{4+} and Mo^{5+} species due to the reduction of Mo oxides
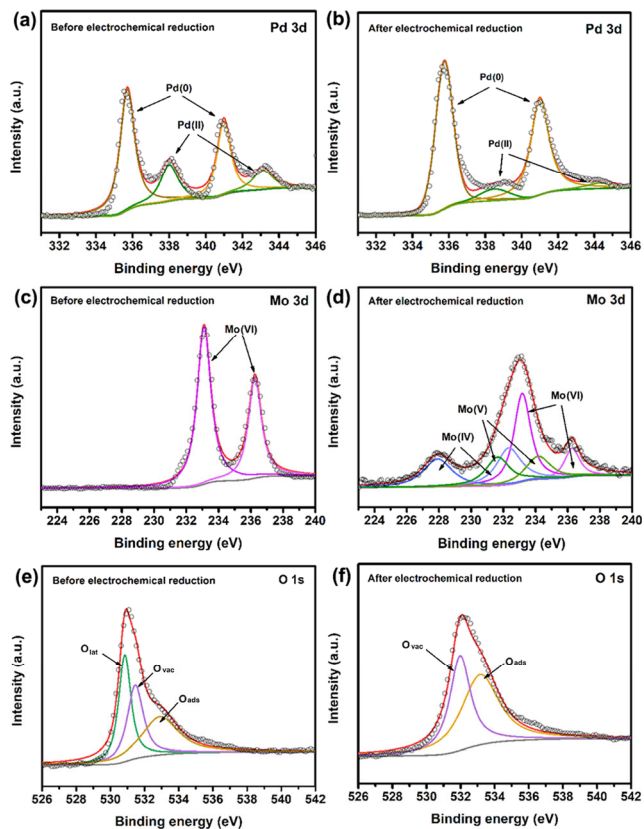

Figure 4 High-resolution XPS (a) and (b) Pd 3d, (c) and (d) Mo 3d, (e) and (f) O 1s spectra of MoO$_x$-Pd/CC before electrochemical reduction and after electrochemical reduction.

at 228.2 and 232.2 eV for Mo^{4+}, and at 231.8 and 234.3 eV for Mo^{5+}, respectively (Fig. 4(d)). However, experimentally obtained Mo^{4+} species has lower binding energy than the reported value (228.8 and 233.1 eV for Mo 3d$_{5/2}$ and Mo 3d$_{3/2}$, respectively) [31]. Shifts in binding energies of Pd and Mo species can be attributed to structural, electronic, and compositional variations of MoO$_x$-Pd/CC. In the O 1s spectrum of Fig. 4(e), the entire peak can be deconvoluted into three distinctive peaks around 530.2, 531.8, and 532.9 eV which are attributed to the lattice oxygen (O$_{lat}$), oxygen vacancy (O$_{vac}$) and surface adsorbed oxygen (O$_{ads}$) [32]. Comparatively, the sample after electrochemical reduction owns more oxygen vacancies and adsorbed oxygen but less lattice oxygen (Fig. 4(f)). Furthermore, ESR, an advanced apparatus for detecting unpaired electrons, was performed on the MoO$_x$-Pd/CC samples to examine the existence of oxygen vacancy. As demonstrated in Fig. S8 in the ESM, the sample without reduction reveals a small signal corresponding to oxygen vacancy spins due to few Mo oxides, especially Mo(V) species as reported by M. Brandhorst and Q. Liu [33, 34], and the signal intensity strengthens after electrochemical reduction, upholding the presumption that the oxygen vacancy concentration in MoO$_x$-Pd/CC samples increases with the transformation of Mo species from high valence (VI) to low valence (IV, V). The experimental results stated above are consistent with Kröger-Vink notation that the existence of Mo^{5+} symbolizes the presence of oxygen vacancies as active sites with a single positive charge [18]. Thereby, the profusion of oxygen defects enables the improved electron transfer and the facilitated adsorption of the active substance, which redounds to the enhancement of HER activity found for MoO$_x$-Pd/CC.

The electrocatalytic activity of MoO$_x$-Pd/CC in 0.5 M H$_2$SO$_4$ for HER was measured by electrochemical measurements, using a typical three-electrode configuration. In comparison,

Pd/CC, MoO$_x$/CC, and commercial Pt mesh were investigated by controlling the same conditions. Figure 5(a) displays the LSV curves of experimental electrodes at a scan rate of 50 mV·s^{-1}. The bare Pd/CC and MoO$_x$/CC electrodes show relatively lower electrocatalytic activity toward HER than MoO$_x$-Pd/CC, which exhibits ultralow overpotential of 25 mV at the current density of 10 mA·cm^{-2} (the overpotential is attained by CP test in Fig. S9 in the ESM), lower than that of commercial Pt mesh (34 mV). Noticeably, there is an obvious reduction peak reflecting Mo species are reduced from high valence to low valence. In contrast, Pd/CC and MoO$_x$/CC show moderate HER activity with higher overpotentials of 78 and 277 mV, respectively. Figure 5(b) illustrates the Tafel plots of MoO$_x$/CC, Pd/CC, MoO$_x$-Pd/CC, and commercial Pt mesh electrodes derived from Fig. 5(a). The Tafel slope for commercial Pt mesh electrode is about 38.68 mV·dec^{-1}, which is compatible with reported values [35]. The MoO$_x$-Pd/CC electrode displays the low Tafel slope of 36.9 mV·dec^{-1}, while the MoO$_x$/CC and Pd/CC electrodes show much larger Tafel slopes of about 110.27 and 81.34 mV·dec^{-1}, respectively. Among them, the MoO$_x$-Pd/CC electrode exhibits the smallest Tafel slope value, revealing that it possesses the highest HER kinetic activity [36, 37]. Generally, the Tafel slope of 120, 40, or 30 mV·dec^{-1} indicates that the reaction rate is determined by Volmer, Heyrovsky, or Tafel step, respectively [38]. Hence, the HER on the MoO$_x$/CC surfaces could proceed via the Volmer-Heyrovsky mechanism and the reaction of the MoO$_x$-Pd/CC electrode is controlled by the Heyrovsky course predominantly. The much higher HER activity of MoO$_x$-Pd/CC is possibly due to the further dispersion of Pd particles and co-existed amorphous MoO$_x$. Because it is suggested that amorphous components could assist both Volmer and Heyrovesky

steps for its reciprocal effect with active groups [20]. Also, the self-supported configuration of MoO$_x$-Pd/CC could accelerate gas spread and electron transport as well, which is conducive to an advanced HER activity.

The EIS analyses were employed to investigate the HER kinetics on the electrode surface at −0.1 V versus RHE. The Nyquist plots of Pd/CC, MoO$_x$/CC, and MoO$_x$-Pd/CC display a near semicircle reflecting the charge transfer resistance, which can be fitted by the analog circuit as demonstrated in Fig. 5(c). The figure shows that MoO$_x$-Pd/CC has a much lower charge transfer resistance (0.56 Ω) than Pd/CC (2.14 Ω) and MoO$_x$/CC (25.27 Ω) [39], confirming that MoO$_x$-Pd/CC provides faster HER kinetics because of progressively dispersed and downsized Pd particles and Mo oxides with more oxygen vacancies, which can effectively upgrade the electrical conductivity of the consequent hybrid electrode. Additionally, the ESCAs of the synthesized catalysts were determined by hydrogen underpotential deposition (HUPD). The CV curves in Fig. S10 in the ESM demonstrated typical Pd/C type of profile with hydrogen adsorption and desorption peaks for Pd/CC and MoO$_x$-Pd/CC [40]. The ECSA of the MoO$_x$-Pd/CC electrocatalyst is calculated to be 105.43 m^2·g^{-1}, which is higher than the Pd/CC electrocatalyst (41.36 m^2·g^{-1}). To investigate the relatively advanced catalytic activity of MoO$_x$-Pd/CC versus Pd/CC, the HER current was normalized by ECSA. As shown in Fig. 5(d), the MoO$_x$-Pd/CC catalyst exhibited higher specific activities than Pd/CC at a series of overpotentials, indicating the superior intrinsic catalytic activity of newly formed MoO$_x$-Pd related species. The electrochemical stability of the MoO$_x$-Pd/CC electrode was further tested by CP in acidic condition at 10 mA·cm^{-2}. As demonstrated in Fig. 5(e) (which has not been corrected by iR compensation), remarkably, the MoO$_x$-Pd/CC electrode not merely maintains quite steady catalytic voltage but even shows a slight decrease of 5 mV in overpotential after 7 days, demonstrating that the exceedingly durable MoO$_x$-Pd/CC can work for HER with excellent stable overpotential [41]. The outstanding stability of MoO$_x$-Pd/CC may be attributed to the formidable connection between MoO$_x$-Pd and CC substrate, avoiding the dissociation of the catalyst during the production of hydrogen. To further investigate the morphologic information of the catalyst after a 7-day operation, the post-HER HRTEM images were obtained for the MoO$_x$-Pd/CC electrode. As exhibited in Fig. S11 in the ESM, ultrasmall Pd nanoparticles with an average size of 2 nm are heavily retained, with negligible degree of aggregation, which explicates that the diminishing overpotential of the MoO$_x$-Pd/CC catalyst is largely influenced by its more exposed active sites. Furthermore, the XRD pattern of the MoO$_x$-Pd/CC catalyst after a 7-day operation is demonstrated in Fig. S12 in the ESM, from which it can be recognized that Pd nanoparticles are miniaturized judging by the enlarged full width at half-maximum of the typical peaks. According to the XPS of the MoO$_x$-Pd/CC catalyst after a 7-day operation (Fig. S13 in the ESM), nearly all of the Pd species become metallic Pd, Mo species of high valence (VI) are further reduced to low valence (IV, V), and O$_{vac}$ turns into the majority part of O 1s. Also, ESR test of the catalyst was executed. As shown in Fig. S14 in the ESM, slightly increased oxygen vacancies are attained for the MoO$_x$-Pd/CC catalyst after a 7-day operation. To sum up, the HER performance of MoO$_x$-Pd/CC (in terms of overpotential, Tafel slope, and stability) is superior to that of most reported electrocatalysts (Table S2 in the ESM). After representing properties and characterizations for the MoO$_x$-Pd/CC sample, it is justified that the increasingly tiny and dispersed Pd particles, along with the enriched oxygen defects and amorphous MoO$_x$, synergistically
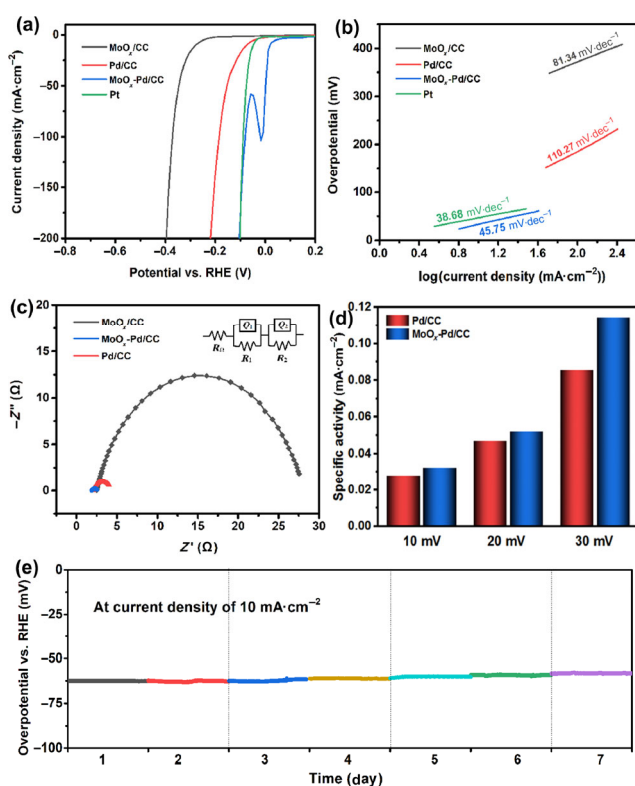

Figure 5 (a) Polarization curves of MoO$_x$/CC, Pd/CC, MoO$_x$-Pd/CC and commercial Pt mesh after *iR*-correction. (b) Corresponding Tafel plots for MoO$_x$/CC, Pd/CC, MoO$_x$-Pd/CC and commercial Pt mesh. (c) Nyquist plots of MoO$_x$/CC, Pd/CC and MoO$_x$-Pd/CC. (d) Specific activities of Pd/CC and MoO$_x$-Pd/CC at overpotentials of 10, 20, and 30 mV in N$_2$ saturated 0.5 M H$_2$SO$_4$. (e) Stability test of MoO$_x$-Pd/CC at a fixed current density of 10 mA·cm^{-2}.

afford the outstanding catalytic activity of MoO$_x$-Pd/CC toward HER.

Moreover, theoretical DFT calculation was also performed to deeply interrogate the impressively improved HER activities of the MoO$_x$-Pd/CC electrode by only introducing trace amorphous MoO$_x$. As displayed by our samples, Mo oxides are stably present in the amorphous membrane due to spontaneous coordinative saturation of the Mo and its strong attraction to O. In the following, we will take MoO$_x$ as an example, and the rationality and reliability of its structure are demonstrated in the supporting information methods and models (Figs. S15 and S16 in the ESM). The difference charge density of calculated MoO$_x$-Pd model (Fig. 6(a)) demonstrated that the interaction between MoO$_x$ and Pd promotes the transfer of electrons from Pd to MoO$_x$. We also mainly calculate the free energy of H$_{ads}$ as the criterion to evaluate HER [42]. Our calculation results (Fig. 6(b)) show that MoO$_x$-Pd (111) has lower reaction barrier of 0.035 eV, with respect to the Pd (111) (0.045 eV). Those results demonstrated that MoO$_x$ adjusts the electronic structure distribution on the surface of Pd(111), and lowers the reaction barrier, thus improving the intrinsic catalytic activity of HER.
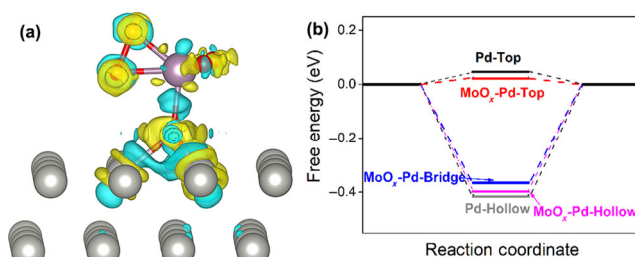

Figure 6 (a) The difference charge density of calculated MoO$_x$-Pd model. (b) Calculated energy changes for the HER at the different sites (top site, bridge site and hollow site) of Pd and MoO$_x$-Pd (111) surfaces.

4 Conclusions

As discussed above, we have displayed a facile engineering strategy rendering large scale manufacture possible to create ultrasmall size Pd nanoparticles with dispersive MoO$_x$ containing oxygen vacancies on common carbon cloth and thus to drastically enhance its HER electrocatalytic properties. We find out that additive amorphous Mo oxides can effectively downsize the Pd crystals and contribute to their further dispersion, at the same time adjust the electronic structure to enhance the catalyst's intrinsic catalytic activity. Benefited from the self-supported formation with superb constructional stability and uniformity, the conductivity and stability of the MoO$_x$-Pd/CC electrode are quite superior whilst the rapid charge transfer rate of that is advantageous for the achievement of favorable reaction kinetics. In consequence, the self-supported MoO$_x$-Pd/CC electrode in 0.5 M H$_2$SO$_4$ only requires an extremely low overpotential of 25 mV to spur a current of 10 mA·cm^{-2}, together with outstanding stability lasting for at least 7 days, which is competitive with the widely-acknowledged commercial catalyst of platinum carbon for electrochemical hydrogen production. Hence, we conceive that this research proposes a novel method for the large scale preparation of electrocatalytic electrode with remarkable HER performance. The high-efficient catalytic properties and the facile preparation approach provide a huge capacity for the utilization of MoO$_x$-Pd/CC in PEM electrolyzers.

Acknowledgements

Electronic Supplementary Material: Supplementary material (XRD patterns, Raman spectra, EDS and HRTEM images, XPS spectra, EPR spectra, CV curves data, etc.) is available in the online version of this article at https://doi.org/10.1007/s12274-020-3083-3.

References

[1] Schlapbach, L.; Züttel, A. Hydrogen-storage materials for mobile applications. *Nature* **2001**, *414*, 353–358.

[2] Eberle, U.; Felderhoff, M.; Schüth, F. Chemical and physical solutions for hydrogen storage. *Angew. Chem., Int. Ed.* **2009**, *48*, 6608–6630.

[3] Yu, P.; Wang, F. M.; Shifa, T. A.; Zhan, X. Y.; Lou, X. D.; Xia, F.; He, J. Earth abundant materials beyond transition metal dichalcogenides: A focus on electrocatalyzing hydrogen evolution reaction. *Nano Energy* **2019**, *58*, 244–276.

[4] Ge, R. X.; Li, L.; Su, J. W.; Lin, Y. C.; Tian, Z. Q.; Chen, L. Ultrafine defective RuO$_2$ electrocatayst integrated on carbon cloth for robust water oxidation in acidic media. *Adv. Energy Mater*. **2019**, *9*, 1901313.

[5] Lei, Y. P.; Wang, Y. C.; Liu, Y.; Song, C. Y.; Li, Q.; Wang, D. S.; Li, Y. D. Designing atomic active centers for hydrogen evolution electrocatalysts. *Angew. Chem., Int. Ed.*, in press, DOI: 10.1002/anie.201914647.

[6] Anjum, M. A. R.; Okyay, M. S.; Kim, M.; Lee, M. H.; Park, N.; Lee, J. S. Bifunctional sulfur-doped cobalt phosphide electrocatalyst outperforms all-noble-metal electrocatalysts in alkaline electrolyzer for overall water splitting. *Nano Energy* **2018**, *53*, 286–295.

[7] Mahmood, N.; Yao, Y. D.; Zhang, J. W.; Pan, L.; Zhang, X. W.; Zou, J. J. Electrocatalysts for hydrogen evolution in alkaline electrolytes: Mechanisms, challenges, and prospective solutions. *Adv. Sci.* **2018**, *5*, 1700464.

[8] Carmo, M.; Fritz, D. L.; Mergel, J.; Stolten, D. A comprehensive review on PEM water electrolysis. *Int. J. Hydrogen Energy* **2013**, *38*, 4901–4934.

[9] Slavcheva, E.; Radev, I.; Bliznakov, S.; Topalov, G.; Andreev, P.; Budevski, E. Sputtered iridium oxide films as electrocatalysts for water splitting via PEM electrolysis. *Electroch. Acta* **2007**, *52*, 3889–3894.

[10] Xu, J.; Zhang, C. X.; Liu, H. X.; Sun, J. Q.; Xie, R. C.; Qiu, Y.; Lü, F.; Liu, Y. F.; Zhuo, L. C.; Liu, X. J. et al. Amorphous MoO$_x$-stabilized single platinum atoms with ultrahigh mass activity for acidic hydrogen evolution. *Nano Energy* **2020**, *70*, 104529.

[11] Zhu, L. L.; Lin, H. P.; Li, Y. Y.; Liao, F.; Lifshitz, Y.; Sheng, M. Q.; Lee, S. T.; Shao, M. W. A rhodium/silicon co-electrocatalyst design concept to surpass platinum hydrogen evolution activity at high overpotentials. *Nat. Commun.* **2016**, *7*, 12272.

[12] Yao, Y. C.; Gu, X. K.; He, D. S.; Li, Z. J.; Liu, W.; Xu, Q.; Yao, T.; Lin, Y.; Wang, H. J.; Zhao, C. M. et al. Engineering the electronic structure of submonolayer Pt on Intermetallic Pd$_3$Pb via charge transfer boosts the hydrogen evolution reaction. *J. Am. Chem. Soc.* **2019**, *141*, 19964–19968.

[13] Smiljanic, M.; Rakocevic, Z.; Maksic, A.; Strbac, S. Hydrogen evolution reaction on platinum catalyzed by palladium and rhodium nanoislands. *Electroch. Acta* **2014**, *117*, 336–343.

[14] Vasić, D. D.; Pašti, I. A.; Mentus, S. V. DFT study of platinum and palladium overlayers on tungsten carbide: Structure and electrocatalytic activity toward hydrogen oxidation/evolution reaction. *Int. J. Hydrogen Energy* **2013**, *38*, 5009–5018.

[15] Bai, S.; Wang, C. M.; Deng, M. S.; Gong, M.; Bai, Y.; Jiang, J.; Xiong, Y. J. Surface polarization matters: Enhancing the hydrogen-evolution reaction by shrinking Pt shells in Pt–Pd–graphene stack structures. *Angew. Chem., Int. Ed.* **2014**, *53*, 12120–12124.

[16] Noerskov, J. K.; Bligaard, T.; Logadottir, A.; Kitchin, J. R.; Chen, J. G.; Pandelov, S.; Stimming, U. Trends in the exchange current for hydrogen evolution. *J. Electrochem. Soc.* 2005, *152*, J23–J26.

[17] Shen, S. Y.; Zhao, T. S.; Xu, J. B.; Li, Y. S. Synthesis of PdNi catalysts for the oxidation of ethanol in alkaline direct ethanol fuel cells. *J. Power Sources* 2010, *195*, 1001–1006.

[18] Ambriz-Peláez, O.; Durón, S.; Olivas, A.; Valdez, R.; Arriaga, L. G.; Álvarez-Contreras, L.; Guerra-Balcázar, M.; Arjona, N. Effect of molybdenum content on the morphology and electronic characteristics of Pd-MoO$_x$ nanomaterials and activity evaluation for ethylene glycol electro-oxidation. *Appl. Surf. Sci.* 2019, *498*, 143842.

[19] Feng, L. G.; Cui, Z. M.; Yan, L.; Xing, W.; Liu, C. P. The enhancement effect of MoO$_x$ on Pd/C catalyst for the electrooxidation of formic acid. *Electroch. Acta* 2011, *56*, 2051–2056.

[20] Chi, K.; Tian, X.; Wang, Q. J.; Zhang, Z. Y.; Zhang, X. Y.; Zhang, Y.; Jing, F.; Lv, Q. Y.; Yao, W.; Xiao, F. et al. Oxygen vacancies engineered CoMoO$_4$ nanosheet arrays as efficient bifunctional electrocatalysts for overall water splitting. *J. Catal.* 2020, *381*, 44–52.

[21] Ma, T. Y.; Dai, S.; Qiao, S. Z. Self-supported electrocatalysts for advanced energy conversion processes. *Mater. Today* 2016, *19*, 265–273.

[22] Mondschein, J. S.; Callejas, J. F.; Read, C. G.; Chen, J. Y. C.; Holder, C. F.; Badding, C. K.; Schaak, R. E. Crystalline cobalt oxide films for sustained electrocatalytic oxygen evolution under strongly acidic conditions. *Chem. Mater.* 2017, *29*, 950–957.

[23] Yang, X. L.; Li, H. N.; Lu, A. Y.; Min, S. X.; Idriss, Z.; Hedhili, M. N.; Huang, K. W.; Idriss, H.; Li, L. J. Highly acid-durable carbon coated Co$_3$O$_4$ nanoarrays as efficient oxygen evolution electrocatalysts. *Nano Energy* 2016, *25*, 42–50.

[24] Ge, R. X.; Wang, S.; Su, J. W.; Dong, Y.; Lin, Y. C.; Zhang, Q. J.; Chen, L. Phase-selective synthesis of self-supported RuP films for efficient hydrogen evolution electrocatalysis in alkaline media. *Nanoscale* 2018, *10*, 13930–13935.

[25] Haddad, N.; Bordes-Richard, E.; Barama, A. MoO$_x$-based catalysts for the oxidative dehydrogenation (ODH) of ethane to ethylene: Influence of vanadium and phosphorus on physicochemical and catalytic properties. *Catal. Today* 2009, *142*, 215–219.

[26] Ressler, T.; Jentoft, R. E.; Wienold, J.; Günter, M. M.; Timpe, O. *In situ* XAS and XRD studies on the formation of mo suboxides during reduction of MoO$_3$. *J. Phys. Chem. B* 2000, *104*, 6360–6370.

[27] He, G. Q.; Song, Y.; Liu, K.; Walter, A.; Chen, S.; Chen, S. W. Oxygen reduction catalyzed by platinum nanoparticles supported on graphene quantum dots. *ACS Catal.* 2013, *3*, 831–838.

[28] Dobrea, I. D.; Ciocan, C. E.; Dumitriu, E.; Popa, M. I.; Petit, E.; Hulea, V. Raman spectroscopy-Useful tool for studying the catalysts derived from Mo and V-oxyanion-intercalated layered double hydroxides. *Appl. Clay Sci.* 2015, *104*, 205–210.

[29] Yan, J. M.; Zhang, X. B.; Han, S.; Shioyama, H.; Xu, Q. Iron-nanoparticle-catalyzed hydrolytic dehydrogenation of ammonia borane for chemical hydrogen storage. *Angew. Chem., Int. Ed.* 2008, *47*, 2287–2289.

[30] Tsukada, C.; Ogawa, S.; Niwa, H.; Nomoto, T.; Kutluk, G.; Namatame, H.; Taniguchi, M.; Yagi, S. Morphological and spectroscopic studies on enlargement of Pd nanoparticle in L-cysteine aqueous solution by AFM and XPS. *Appl. Surf. Sci.* 2013, *267*, 48–52.

[31] Choi, J. G.; Thompson, L. T. XPS study of as-prepared and reduced molybdenum oxides. *Appl. Surf. Sci.* 1996, *93*, 143–149.

[32] Sun, P.; Wang, B. Q.; Zhao, L. P.; Gao, H. Y.; Wang, T. S.; Yang, X. L.; Liu, C.; Lu, G. Y. Enhanced gas sensing by amorphous double-shell Fe$_2$O$_3$ hollow nanospheres functionalized with PdO nanoparticles. *Sens. Actuators B Chem.* 2017, *252*, 322–329.

[33] Brandhorst, M.; Cristol, S.; Capron, M.; Dujardin, C.; Vezin, H.; Le Bourdon, G.; Payen, E. Catalytic oxidation of methanol on Mo/Al$_2$O$_3$ catalyst: An EPR and Raman/infrared operando spectroscopies study. *Catal. Today* 2006, *113*, 34–39.

[34] Liu, Q. W.; Wu, Y. W.; Zhang, J. W.; Chen, K. J.; Huang, C. J.; Chen, H.; Qiu, X. Q. Plasmonic MoO$_{3−x}$ nanosheets with tunable oxygen vacancies as efficient visible light responsive photocatalyst. *Appl. Surf. Sci.* 2019, *490*, 395–402.

[35] Jiang, B. B.; Yang, L. L.; Liao, F.; Sheng, M. Q.; Zhao, H. Z.; Lin, H. P.; Shao, M. W. A stepwise-designed Rh-Au-Si nanocomposite that surpasses Pt/C hydrogen evolution activity at high overpotentials. *Nano Res.* 2017, *10*, 1749–1755.

[36] Lu, H. Y.; Fan, W.; Huang, Y. P.; Liu, T. X. Lotus root-like porous carbon nanofiber anchored with CoP nanoparticles as all-pH hydrogen evolution electrocatalysts. *Nano Res.* 2018, *11*, 1274–1284.

[37] Pan, Y.; Zhang, C.; Lin, Y.; Liu, Z.; Wang, M. M.; Chen, C. Electrocatalyst engineering and structure-activity relationship in hydrogen evolution reaction: From nanostructures to single atoms. *Sci. China Mater.* 2020, *63*, 921–948.

[38] Yan, X. D.; Tian, L. H.; Atkins, S.; Liu, Y.; Murowchick, J.; Chen, X. B. Converting CoMoO$_4$ into CoO/MoO$_x$ for overall water splitting by hydrogenation. *ACS Sustainable Chem. Eng.* 2016, *4*, 3743–3749.

[39] Geng, S.; Liu, Y. Q.; Yu, Y. S.; Yang, W. W.; Li, H. B. Engineering defects and adjusting electronic structure on S doped MoO$_2$ nanosheets toward highly active hydrogen evolution reaction. *Nano Res.* 2020, *13*, 121–126.

[40] Luo, M. C.; Zhao, Z. L.; Zhang, Y. L.; Sun, Y. J.; Xing, Y.; Lv, F.; Yang, Y.; Zhang, X.; Hwang, S.; Qin, Y. N. et al. PdMo bimetallene for oxygen reduction catalysis. *Nature* 2019, *574*, 81–85.

[41] Lu, S. J.; Wang, W. J.; Yang, S. S.; Chen, W.; Zhuang, Z. B.; Tang, W. J.; He, C. H.; Qian, J. J.; Ma, D. K.; Yang, Y. et al. Amorphous MoS$_2$ confined in nitrogen-doped porous carbon for improved electrocatalytic stability toward hydrogen evolution reaction. *Nano Res.* 2019, *12*, 3116–3122.

[42] Zhu, J. Q.; Wang, Z. C.; Dai, H. J.; Wang, Q. Q.; Yang, R.; Yu, H.; Liao, M. Z.; Zhang, J.; Chen, W.; Wei, Z. et al. Boundary activated hydrogen evolution reaction on monolayer MoS$_2$. *Nat. Commun.* 2019, *10*, 1348.